Dual-Loop Continuous Control Set Model-Predictive Control for a Three-Phase Unity Power Factor Rectifier

Carlos Alfaro, Ramon Guzman, *Member, IEEE*, Luis Garcia de Vicuña, Jaume Miret, *Member, IEEE*, and Miguel Castilla

***Abstract*—In this article, a novel cascade model-predictive control for a three-phase unity power factor rectifier is presented. Unlike the traditional control techniques for rectifiers, the proposed method uses a cascade dual-model-predictive control for the inner and outer control loops. The three-phase currents of the rectifier are controlled with the inner control loop, while the desired output voltage is achieved with the outer control loop. In this proposal, the output power is used as a feedforward to enhance the transient dynamics of the output dc voltage. Several advantages can be highlighted such as a fixed switching frequency, and output voltage variations are avoided when a sudden change in the load or a voltage sag appears. The overall control proposal has been fully integrated into a digital signal processor. Selected experimental results are introduced to validate the theoretical contributions of this article.**

***Index Terms*—Current control, Kalman filter (KF), model-predictive control (MPC), rectifier.**

I. Introduction

TRADITIONALLY, three-phase rectifiers have been used as an interface between a three-phase system and the ac line in electronic equipment supplied with a dc voltage. The three-phase diode bridge rectifiers are widely used to convert ac to dc [1]. Notwithstanding, these systems exhibit a low power factor (PF) and inject current harmonics to the grid. These facts may cause nondesirable effects such as an increase in the power supply voltage distortion and even the damage of the rectifier due to overheating. As an alternative, a unity power factor rectifier (UPFR) is a better solution. A high PF and a fast dynamic response of the output voltage can be achieved if a proper control algorithm is implemented [2], [3].

Manuscript received March 4, 2021; revised May 14, 2021 and July 12, 2021; accepted August 19, 2021. Date of publication August 24, 2021; date of current version October 15, 2021. This work was supported in part by the Ministry of Science, Innovation and Universities of Spain and in part by the European Regional Development Fund under Project RTI2018-100732-B-C22. Recommended for publication by Associate Editor P. Mattavelli. *(Corresponding author: Carlos Alfaro.)*

Carlos Alfaro, Luis Garcia de Vicuña, Jaume Miret, and Miguel Castilla are with the Department of Electronic and Electrical Engineering, Technical University of Catalonia, 08800 Vilanova i la Geltrú, Spain (e-mail: carlos.arturo.alfaro@upc.edu; vicuna@eel.upc.edu; jaume.miret@upc.edu; miquel.castilla@upc.edu).

Ramon Guzman is with the Department of Automatic Control, Technical University of Catalonia, 08800 Vilanova i la Geltrú, Spain (e-mail: ramon.guzman@upc.edu).

Color versions of one or more figures in this article are available at https://doi.org/10.1109/TPEL.2021.3107221.

Digital Object Identifier 10.1109/TPEL.2021.3107221

The cascade control structure in the UPFR is widely used since the dc-link voltage and the ac current dynamics can be separated in a zero dynamics concept based on two time scales: one with slow dynamics and the other with fast dynamics.

In UPFR application, the cascade structure is widely used since the dc-link voltage and the ac current dynamics can be separated in two time scales, formed by an outer loop (voltage loop) and an inner loop (current loop) [4], [5]. The inner loop is intended to track the grid currents to achieve a high PF, and the outer loop, usually a proportional–integral (PI) controller, is designed to obtain the desired output voltage. Focusing on the inner loop, many control methods have been proposed in order to achieve high dynamic performances and robustness, such as sliding-mode control [6]–[8], dead-beat control [9], [10], direct power control [11], [12], and model-predictive control (MPC) [13]–[19].

In recent years, with the development of digital signal processors (DSPs), the MPC has attracted more and more attention in some industrial fields such as power electronics or electrical systems, among others [13]–[28]. The MPC is greatly suitable for controlling power converters due to its intrinsic characteristics, such as fast transient response, high control bandwidth, and providing a straightforward way of including system nonlinearities and constraints [13]–[26].

There exist two different control strategies regarding MPC algorithms for three-phase power converters: the finite-control-set model-predictive control (FCS-MPC) [14]–[22] and the continuous-control-set model-predictive control (CCS-MPC) [23]–[26]. In the FCS-MPC, a cost function is minimized for every switching state. This control method uses a comparator instead of a modulator to decide the optimum switching pattern to be applied. As a consequence, the switching frequency is variable, requiring an increment in the sampling frequency and the computational burden. Conversely, in the CCS-MPC, the control algorithm is based on the prediction of state variables using a discrete model of the converter. In regard to this technique, a cost function is minimized inside a predictive window to obtain the vector of future control actions. Moreover, based on the receding horizon concept, only the first value of this vector is used in a space vector modulator (SVM) leading to a fixed switching frequency. This fact provides a reduction in the sampling frequency and, as a consequence, in the computational burden [29].

Recently, the FCS-MPC has been applied in UPFR controllers [15]–[19]. In [15], a single-loop FCS-MPC method is applied to control both the dc-link voltage and the active and reactive powers. However, since the active power reference is calculated based on the system model, an extra integrator is required to correct the steady-state error caused by the inevitable parameter mismatch, deteriorating the disturbance rejection properties and the stability robustness. Moreover, in most applications, dc-link capacitors are large; thus, the output voltage dynamic has a larger time constant as compared with the ac current loop. Otherwise, in [16]–[18], cascade control loops are applied using FCS-MPC as the inner loop, while the outer loop control has not yet attracted plenty of consideration with PI control being the most usual strategy. In [16], a detailed description of FCS-MPC is presented, where the active and reactive powers of the system are directly controlled. However, as mentioned above, the FCS-MPC is based on the use of comparators, which provokes a variable switching frequency increasing the switching noise. It should be noted that this method has a high sensitivity against measurement noise and parameter uncertainties. In [17], a grid voltage sensorless FCS-MPC based on virtual-flux-based grid voltage estimation is presented. This approach can operate in the presence of voltage sags and under distorted network conditions. However, since the outer loop has been addressed using a classic PI controller, the output voltage is very sensitive to sudden load changes. Moreover, robustness against system parameter uncertainties is not tested. In [18], a sensorless FCS-MPC with a model reference adaptive system (MRAS) estimator is proposed. The main advantage of this approach is the accurate grid inductance estimation and the robustness against parameter uncertainties. However, the outer loop has been addressed using a classic PI controller, which can degrade the output voltage dynamic performances in the case of sudden load changes. It should be noted that this approach is not tested in the presence of voltage sags. Instead, in [19], a cascade FCS-MPC is presented in order to improve the voltage dynamic transient response. In this approach, grid currents and output voltage errors are used in two different cost functions for the inner and outer loops, respectively. The main drawback of this control method is that the output voltage is very sensitive against measurement noise, as mentioned in [19]. Moreover, this approach is not tested in the presence of voltage sags.

However, since PI controllers are tuned based on an operation point, the performance and dynamic response of the system is degraded in the presence of external disturbances, as is the case of sudden load changes [8]. Instead, the wider control bandwidth is more likely to be achieved by MPC for the absence of stability-related compromises in the tuning stage [35].

Unlike other aforementioned methods for UPFRs, this article proposes a novel cascade CCS-MPC for both inner and outer control loops. On the one hand, the use of this technique in the inner loop avoids the use of proportional integral (PI) or proportional resonant (PR) controllers to generate control signals, avoiding the disturbance sensitivity associated with these controllers [30]. Moreover, a continuous duty cycle is obtained, which allows using an SVM; thus, a fixed switching frequency is achieved. The model is also used in a Kalman filter (KF) to estimate three-phase grid currents and provide robustness against noisy environments. On the other hand, focusing on the outer loop, PI controllers are widely used in the dc-link voltage control. However, since PI controllers are tuned based on an operation point, the performance and the dynamic response of the system are degraded in the presence of external disturbances, as is the case of sudden load changes [8]. Instead, the MPC can achieve a wider control bandwidth due to the absence of stability compromises in the tuning stage [31]. Therefore, the usual PI controller, used for the outer loop, is replaced by a second MPC. With this proposal, the dynamic performance of the output voltage in case of load changes and voltage sags is improved, making the system less sensitive to these disturbances. Finally, compared to a single-loop controller, the cascade control system has several advantages, such as disturbance rejection and robustness against model parameter uncertainties [32], [33].

The novelty of this article is the use of two CCS-MPCs in a cascade way. To do so, the model of the rectifier is divided into two linear models, where two different cost functions are defined for inner and outer loops, respectively. Since it is an unconstrained problem, the cost functions can be minimized offline, reducing the computational burden [29]. The main contributions can be summarized as follows.

1) The use of a linear model in a unconstrained CCS-MPC allows a reduction in the computational burden.
2) Robustness of the output voltage over sudden load changes.
3) Robustness against model parameter uncertainties.
4) The controller operates satisfactorily even in the case of grid voltage sags.
5) A fixed switching frequency is achieved.
6) A low total harmonic distortion (THD) of the grid currents is achieved.

The rest of this article is organized as follows. Section II introduces the linear model of the UPFR. In Section III, the proposed MPC system is presented. Section IV deals with the controller implementation. In Section V, the controller design is presented. Section VI deals with stability and robustness analysis, while the experimental results are reported in Section VII. Finally, Section VIII concludes this article.

II. Modeling the UPFR in the dq Coordinates

The electrical circuit of a UPFR is shown in Fig. 1. The differential equations in the dq reference frame can be written as follows:

$$L\frac{di_d}{dt} = v_d + \omega L i_q - m_d\frac{v_o}{2} \tag{1}$$

$$L\frac{di_q}{dt} = v_q - \omega L i_d - m_q\frac{v_o}{2} \tag{2}$$

$$C\frac{dv_o}{dt} = \frac{3}{2}\left(m_d i_d + m_q i_q\right) - i_o \tag{3}$$

where i_d, i_q and v_d, v_q are the dq components of the grid currents i_a, i_b, and i_c and the grid voltages v_a, v_b, and v_c, respectively. The control signals are represented by m_d and m_q, v_o is the output voltage, and ω is the grid angular frequency.

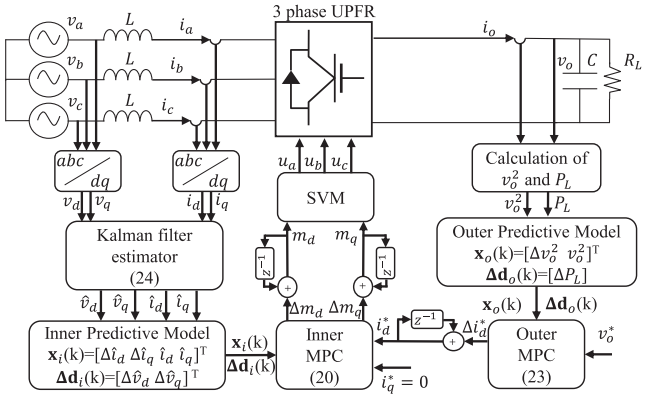

Fig. 1. Circuit diagram and proposed control of the three-phase UPFR.

In this article, a cascade CCS-MPC is proposed. In order to apply a cascade CCS-MPC, the above model is divided into two parts. Equations (1) and (2) will be used to design the predictive controller for the inner loop, while (3) for the output loop. The design of these controllers will be shown in the next sections.

III. Proposed Control System

This section presents the proposed control system. In order to achieve the control objective presented in the following, this article proposes a cascade CCS-MPC. The main control objective is to guarantee sinusoidal input currents in phase with the grid voltages. Besides, the second objective is to regulate the output voltage to the desired nominal value. Finally, the third objective is to bring robustness against external disturbances, such as load changes and grid voltage sags.

Fig. 1 shows the proposed cascade controller for the UPFR. As shown in the figure, the controller consists of two MPC loops. On the one hand, the outer-loop-predicted variables and disturbance vectors are obtained using the square output dc-link voltage and the output power. These variables together with the output dc-link voltage reference are the inputs of the outer MPC. As usual, in a cascade controller, the output of the outer controller is the reference of the inner controller [32], [33]. Taking this in mind, the outer loop regulates the output dc-link voltage generating the reference currents used by the inner loop. On the other hand, for the inner loop, three-phase voltages and currents are transformed into the dq reference frame and are applied to a KF to estimate the grid-side currents and voltages to provide robustness against noisy environments. Then, current and voltage estimations are used to generate the inner-loop-predicted variables and disturbances vectors. The inner MPC uses these variables and the reference currents generated by the outer loop to obtain the control signals. Finally, the control signals are used by an SVM, thus providing a fixed switching frequency, opposite to other MPC techniques such as FCS-MPC.

A. Proposed Linear Discrete Model for the Inner Control Loop

This section deals with the proposed linear predictive model to be used in the inner controller. As stated in Section II, the discrete model can be obtained from (1) and (2) as follows:

$$i_d(k+1) = i_d(k) + \frac{T_s}{L}v_d(k) + \omega T_s i_q(k) - m_d\frac{T_s v_o}{2L} \quad (4)$$

$$i_q(k+1) = i_q(k) + \frac{T_s}{L}v_q(k) - \omega T_s i_d(k) - m_q\frac{T_s v_o}{2L} \quad (5)$$

where T_s is the sampling period.

Taking into account that the output voltage is a slow variable, v_o can be considered constant in a sampling period T_s. With these considerations, (4) and (5) can be represented as a linear model. Moreover, the dynamics of the grid voltages may be unknown, for instance, in the case of sags. Then, it is proposed to separate the grid voltages from the model described by (4) and (5) while considering those voltages as disturbances. However, v_d and v_q are suitable to be used as feedforward terms to improve the dynamics of the current and bring robustness against grid voltage variations, as it will be demonstrated in Section VII. Finally, the current linear model can be represented by the following state-space equations:

$$\mathbf{x}_{m,i}(k+1) = \mathbf{A}_{m,i}\mathbf{x}_{m,i}(k) + \mathbf{B}_{m,i}\mathbf{u}_i(k) + \mathbf{D}_{m,i}\mathbf{d}_i(k) \quad (6)$$

$$\mathbf{y}_i(k) = \mathbf{C}_{m,i}\mathbf{x}_{m,i}(k) \quad (7)$$

where the subindex i is used to refer the inner controller. The grid current vector, the control signal vector, and the grid voltage vector in the dq frame are expressed by $\mathbf{x}_{m,i} = [i_d \;\; i_q]$, $\mathbf{u}_i = [m_d \;\; m_q]$, and $\mathbf{d}_i = [v_d \;\; v_q]$, respectively, and

$$\mathbf{A}_{m,i} = \begin{pmatrix} 1 & \omega T_s \\ -\omega T_s & 1 \end{pmatrix}, \quad \mathbf{B}_{m,i} = \begin{pmatrix} -\frac{v_o T_s}{2L} & 0 \\ 0 & -\frac{v_o T_s}{2L} \end{pmatrix}$$

$$\mathbf{D}_{m,i} = \begin{pmatrix} \frac{T_s}{L} & 0 \\ 0 & \frac{T_s}{L} \end{pmatrix}, \quad \mathbf{C}_{m,i} = \begin{pmatrix} 1\,0 \\ 0\,1 \end{pmatrix}.$$

Now, in order to eliminate the steady-state error, an integrator is embedded in the model. To this aim, (6) can be expressed according to Appendix A as follows:

$$\mathbf{x}_i(k+1) = \mathbf{A}_i\mathbf{x}_i(k) + \mathbf{B}_i\Delta\mathbf{u}_i(k) + \mathbf{D}_i\Delta\mathbf{d}_i(k) \quad (8)$$

$$\mathbf{y}_i(k) = \mathbf{C}_i\mathbf{x}_i(k) \quad (9)$$

where $\mathbf{x}_i(k) = [\Delta\mathbf{x}_{m,i}(k) \;\; \mathbf{y}_i(k)]^T$ and the matrices of the augmented model $\mathbf{A}_i$, $\mathbf{B}_i$, $\mathbf{C}_i$, and $\mathbf{D}_i$ can be computed according to Appendix A as a function of the matrices $\mathbf{A}_{m,i}$, $\mathbf{B}_{m,i}$, $\mathbf{C}_{m,i}$, and $\mathbf{D}_{mi}$, yielding

$$\mathbf{A}_i = \begin{pmatrix} 1 & \omega T_s & 0 & 0 \\ -\omega T_s & 1 & 0 & 0 \\ 1 & \omega T_s & 1 & 0 \\ -\omega T_s & 1 & 0 & 1 \end{pmatrix}, \quad \mathbf{B}_i = \begin{pmatrix} -\frac{v_o T_s}{2L} & 0 \\ 0 & -\frac{v_o T_s}{2L} \\ -\frac{v_o T_s}{2L} & 0 \\ 0 & -\frac{v_o T_s}{2L} \end{pmatrix}$$

$$\mathbf{C}_i = \begin{pmatrix} 0\,0\,1\,0 \\ 0\,0\,0\,1 \end{pmatrix}, \quad \mathbf{D}_i = \begin{pmatrix} \frac{T_s}{L} & 0 \\ 0 & \frac{T_s}{L} \\ \frac{T_s}{L} & 0 \\ 0 & \frac{T_s}{L} \end{pmatrix}.$$

B. Proposed Discrete Model for the Outer Control Loop

A linear predictive model for the outer loop is presented in this section. The zero dynamics concept [34] is applied to obtain the dynamics of the output voltage, v_o. The output voltage zero dynamics is the dynamics of v_o when the inner loop is established (i.e., $i_d = i_d^*$ and $i_q = 0$), since a unity PF is achieved. Then, according to this principle, the current component i_d can be substituted into (3) by the current reference of the inner loop i_d^*. Moreover, the duty cycle m_d can be obtained from (1) by considering that all parasitic resistances and inductances are neglected and a quasi-steady-state approach (i.e., assuming that the first derivative of i_d is negligible)

$$m_d = \frac{2v_d}{v_o}. \tag{10}$$

With these considerations, and using (10) in (3), we obtain

$$C\frac{dv_o}{dt} = 3\frac{v_d}{v_o}i_d^* - i_o \tag{11}$$

or equivalently

$$\frac{C}{2}\frac{dv_o^2}{dt} = 3v_d i_d^* - P_L \tag{12}$$

where P_L is the power delivered to the load. In the previous equation, v_d can be considered as a parameter (i.e., the peak value of the nominal grid voltage). Note that (12) is a linear differential equation with respect to v_o^2. Then, if (12) is discretized, then

$$v_o^2(k+1) = v_o^2(k) + \frac{6T_s v_d}{C}i_d^*(k) - \frac{2T_s}{C}P_L(k). \tag{13}$$

On the other hand, the dynamics of P_L is unknown, and in a similar way that is explained in the last section, this variable can be separated from the model described by (13) and considered as a disturbance. Alternatively, in this article, P_L is used as a feedforward term in the outer control loop. As will be presented in Section V, the reference current is generated by including a measurement of the output power, thus rapidly changing this reference according to changes in load. In this way, this additional term substantially reduces the sensitivity of the output voltage over sudden load changes, as will be seen in Section VII. Taking into account these considerations, the predictive model for the outer controller can be defined with the following state-space equations:

$$x_{m,o}(k+1) = A_{m,o}x_{m,o}(k) + B_{m,o}u_o(k) + D_{m,o}d_o(k) \tag{14}$$

$$y_o(k) = C_{m,o}x_{m,o}(k) \tag{15}$$

where the subindex o is used to refer the outer controller, being

$$x_{m,o} = v_o^2,\ u_o = i_d^*,\ d_o = P_L$$

$$A_{m,o} = 1,\ B_{m,o} = \frac{6T_s v_d}{C},\ C_{m,o} = 1,\ D_{m,o} = \frac{2T_s}{C}.$$

This model can be rewritten in its incremental form in order to embed an integrator, yielding

$$\mathbf{x}_o(k+1) = \mathbf{A}_o\mathbf{x}_o(k) + \mathbf{B}_o u_o(k) + \mathbf{D}_o\Delta d_o(k) \tag{16}$$

$$y_o(k) = \mathbf{C}_o\mathbf{x}_o(k) \tag{17}$$

where $\mathbf{x}_o(k) = [\Delta x_{m,o}(k) \quad y_o(k)]^T$ and the matrices of the augmented model $\mathbf{A}_o$, $\mathbf{B}_o$, $\mathbf{C}_o$, and $\mathbf{D}_o$ can be obtained from $A_{m,o}$, $B_{m,o}$, $C_{m,o}$, and $D_{m,o}$, as shown in Appendix A:

$$\mathbf{A}_o = \begin{pmatrix} 1 & 0 \\ 1 & 1 \end{pmatrix}, \quad \mathbf{B}_o = \begin{pmatrix} \frac{6T_s v_d}{C} \\ \frac{6T_s v_d}{C} \end{pmatrix}$$

$$\mathbf{C}_o = \begin{pmatrix} 0 & 1 \end{pmatrix}, \quad \mathbf{D}_o = \begin{pmatrix} \frac{2T_s}{C} \\ \frac{2T_s}{C} \end{pmatrix}.$$

C. Inner Control Loop

The inner controller is designed using the following cost function:

$$\mathbf{J}_i = (\mathbf{y}_i^* - \mathbf{y}_i)^T(\mathbf{y}_i^* - \mathbf{y}_i) + \Delta\mathbf{u}_i^T\mathbf{R}_i\Delta\mathbf{u}_i \tag{18}$$

where $\mathbf{R_i} = r_{\omega,i}\mathbf{I}_{2N_{c,i}\times 2N_{c,i}}$ is a diagonal matrix with $r_{\omega,i} > 0$. The control effort is used as a tuning parameter to adjust a desired closed-loop performance, and $N_{c,i}$ is the control horizon for the inner controller. Considering that the reference current is maintained practically constant inside a predictive window, $N_{p,i}$, $\mathbf{y}_i^*$ can be expressed according to Appendix B as follows:

$$\mathbf{y}_i^* = [\underbrace{\mathbf{I}_{2\times 2} \ \ \mathbf{I}_{2\times 2} \ \ \ldots \ \ \mathbf{I}_{2\times 2}}_{N_{p,i}}]y_i^*(k_j) \tag{19}$$

where k_j is the instant of time at which the control signal vector is calculated. Besides, $y_i^*(k_j) = [i_d^* \ \ i_q^*]$ is the reference current vector at the sampling instant k_j, and $\mathbf{I}_{2\times 2}$ is the identity matrix with size 2×2 repeated as many times as the prediction horizon $N_{p,i}$. Note that it should be accomplished that $i_q^* = 0$ in order to achieve a unity PF.

In the unconstrained problem, the optimization of (18) can be solved analytically (offline). As a result, a vector of incremental control signals is obtained: $\Delta\mathbf{u}_i = [\Delta\mathbf{u}_i(k_j), \Delta\mathbf{u}_i(k_j+1), \ldots, \Delta\mathbf{u}_i(k_j+N_c-1)]$. According to the receding horizon principle, only the first component of this vector is used to generate the control signal. Then, the actual incremental control signal for the inner loop is

$$\Delta\mathbf{u}_i(k_j) = \mathbf{K}_{r,i}y_i^*(k_j) - \mathbf{K}_{c,i}\mathbf{x}_i(k_j) - \mathbf{K}_{h,i}\Delta\mathbf{d}_i(k_j) \tag{20}$$

where $\mathbf{K}_{r,i}$, $\mathbf{K}_{c,i}$, and $\mathbf{K}_{h,i}$ are the gains of the inner controller. A detailed procedure of how these gains are obtained can be found in Appendix B. Note that the disturbance vector is the grid voltage vector, i.e., $\mathbf{d}_i = [v_d \ \ v_q]$. By considering this disturbance vector in the minimization procedure, the inner loop will be robust against grid voltage variations, for instance, in the case of voltage sags. Finally, the control signal applied to the converter, $\mathbf{u}_i(k_j)$, is obtained as $\mathbf{u}_i(k_j) = \mathbf{u}_i(k_j - 1) + \Delta\mathbf{u}_i(k_j)$.

D. Outer Control Loop

The outer controller is designed using the same cost function as explained before

$$\mathbf{J}_o = (\mathbf{y}_o^* - \mathbf{y}_o)^T(\mathbf{y}_o^* - \mathbf{y}_o) + \Delta\mathbf{u}_o^T\mathbf{R}_o\Delta\mathbf{u}_o \tag{21}$$

where $\mathbf{R_o} = r_{\omega,o}\mathbf{I}_{N_{c,o}\times N_{c,o}}$ is a diagonal matrix with $r_{\omega,o} > 0$. The control effort is used as a tuning parameter to adjust a desired closed-loop performance of the desired dynamics of the

output voltage v_o, and $N_{c,o}$ is the control horizon for the outer controller.

As has been explained in the previous section, the reference voltage can be expressed as follows:

$$\mathbf{y}_o^* = [\underbrace{1 \;\; 1 \;\; \dots \;\; 1}_{N_{p,o}}]^T y_o^*(k_j) \tag{22}$$

where, according to (13), $y_o^*(k_j) = (v_o^*)^2$ is the reference squared voltage at the sampling instant k_j. Note that the size of vector $\mathbf{y}_o^*$ is given by the prediction horizon $N_{p,o}$.

If (21) is minimized, a vector of optimum control signals is obtained and defined as

$$\Delta \mathbf{u}_o(k_j) = \mathbf{K}_{r,o} y_o^*(k_j) - \mathbf{K}_{c,o}\mathbf{x}_o(k_j) - K_{h,o}\Delta d_o(k_j) \tag{23}$$

where $\mathbf{K}_{r,o}$, $\mathbf{K}_{c,o}$, and $K_{h,o}$ are the gains of the outer controller. In this article, the control signal obtained from the outer controller is used as the reference current by the inner controller, $i_d^*(k)$. Then, assuming that the inner control loop is established, the vector of the incremental references is defined as $\Delta \mathbf{u}_o = [\Delta i_d^*(k_j), \Delta i_d^*(k_j+1), \dots, \Delta i_d^*(k_j+N_{c,o}-1)]$. Once again, if the receding horizon principle is used, only the first value of this vector is considered, and $i_d^*(k_j)$ is obtained as $i_d^*(k_j) = i_d^*(k_j-1) + \Delta i_d^*(k_j)$.

E. State Estimation

In order to obtain the state-space vector of the inner loop defined in (4) and (5), the current components are estimated. The state variable for the inner loop has been estimated by using a KF as follows:

$$\begin{aligned}\hat{\mathbf{x}}_{m,i}(k+1) = {} & \mathbf{A}_{m,i}\hat{\mathbf{x}}_{m,i}(k) + \mathbf{B}_{m,i}u_i(k) \\ & + \mathbf{D}_{m,i}d_i(k) + \mathbf{L}_{\text{obs}}(y_i(k) - \mathbf{C}_{m,i}\hat{\mathbf{x}}_{m,i}(k))\end{aligned} \tag{24}$$

where $\mathbf{L}_{\text{obs}}$ is the observer gain, which has been adjusted according to the KF algorithm [35]. The main feature provided by the KF in this application is that all the variables used in the control algorithm are estimated and free of noise. Besides, the KF generates a filtered signal of the grid currents improving the system performance.

IV. Closed-Loop System

In this section, the closed-loop system is analyzed. In Section III-C, it has been shown that the optimum incremental control signal value at the sampling instant k_j is defined in Appendix B by (58). If the disturbance term $\mathbf{K}_h$ is not considered for the stability analysis, (58) can be rewritten as

$$\Delta u(k) = \mathbf{K}_r y^*(k) - \mathbf{K}_c \mathbf{x}(k). \tag{25}$$

Now, to prove the effect of the predictive control in the system dynamics, (25) is replaced in (44)

$$\mathbf{x}(k+1) = \mathbf{A}\mathbf{x}(k) - \mathbf{B}\mathbf{K}_c\mathbf{x}(k) - \mathbf{K}_r\mathbf{B}y^*(k) \tag{26}$$

or equivalently

$$\mathbf{x}(k+1) = (\mathbf{A} - \mathbf{B}\mathbf{K}_c)\mathbf{x}(k) - \mathbf{K}_r\mathbf{B}y^*(k) \tag{27}$$

TABLE I
System Parameters

Description	Symbol	Value
Grid voltage	V_{grid}	50 V_{rms}
Grid frequency	f	60 Hz
Nominal dc-link voltage	V_o	220 V
Nominal dc capacitor	C	1000 uF
Grid inductance	L	5 mH
Sampling frequency	f_s	10 kHz
Switching frequency	f_{sw}	10 kHz
Inner loop prediction horizon	$N_{p,i}$	8
Inner loop control horizon	$N_{c,i}$	4
Inner loop control effort	$r_{\omega,i}$	2
Outer loop prediction horizon	$N_{p,o}$	400
Outer loop control horizon	$N_{c,o}$	80
Outer loop control effort	$r_{\omega,o}$	3×10^9

where the closed-loop eigenvalues can be obtained by solving the determinant

$$|\mathbf{A} - \mathbf{B}\mathbf{K}_c - \lambda\mathbf{I}| = 0. \tag{28}$$

The eigenvalues have a dependence of $\mathbf{K}_c$ and, as a consequence, of $\mathbf{R}$. As evidenced by the last expression, by selecting the appropriate value of $\mathbf{R}$ in (58), a desired dynamics of the MPC can be obtained. Equation (28) is computed for both loops using corresponding parameters $\mathbf{A}_i, \mathbf{B}_i$, and $\mathbf{K}_{c,i}$ for the inner and $\mathbf{A}_o, \mathbf{B}_o$, and $\mathbf{K}_{c,o}$ for the outer. Table I shows the controller parameters for both loops. The inner loop control effort $r_{\omega,i}$ is chosen to obtain a fast transient response. Moreover, the outer loop control effort $r_{\omega,o}$ is chosen to obtain a slower transient response than the inner loop.

A. Design Guidelines

This subsection presents the design procedure of the proposed cascade CCS-MPC parameters $r_{\omega,i}$ and $r_{\omega,o}$, which correspond to the control effort of the inner and outer loops, respectively. The control parameters are designed according to the dynamic specification using the closed-loop poles as a function of $r_{\omega,i}$ for the inner loop and $r_{\omega,o}$ for the outer loop.

First, focusing on the inner loop, the parameter $r_{\omega,i}$ is designed considering the compromise between the settling time and the maximum deviation during transients according to the following specifications.

1) To guarantee stability, the prediction and control horizons, $N_{p,i}$ and $N_{c,i}$, have to be designed large enough [31].
2) To guarantee a good transient response, the settling time is designed less than 1 ms.
3) To achieve a good dynamic response with low overshoots, the dominant poles must be placed with a damping ratio close to 0.707 [36].

Second, the outer loop control effort $r_{\omega,o}$ must be adjusted to ensure a smooth reference current and a high dynamic performance. Taking this in mind, the outer loop parameter is designed according to the following specification.

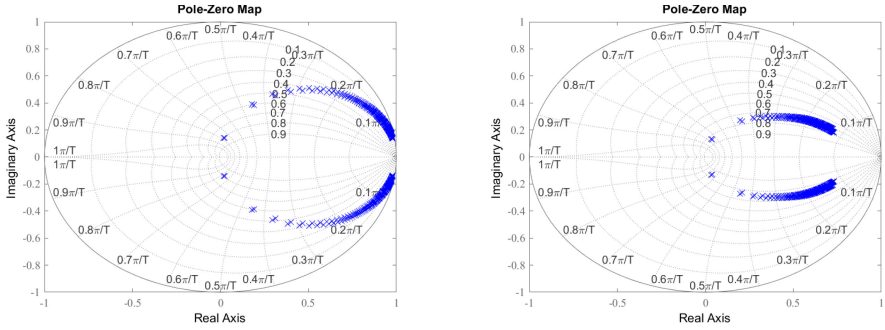

(a) (b)

Fig. 2. Inner closed-loop poles for $r_{\omega,i}$ variation from 0 to 100. (a) $N_{p,i} = 2$ and $N_{c,i} = 1$. (b) $N_{p,i} = 8$ and $N_{c,i} = 4$.

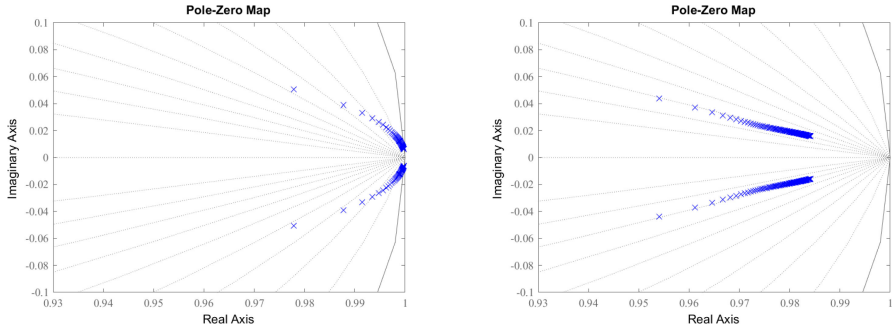

(a) (b)

Fig. 3. Outer closed-loop poles for $r_{\omega,o}$ variation from 10^6 to 10^{10}. (a) $N_{p,o} = 40$ and $N_{c,o} = 8$. (b) $N_{p,o} = 400$ and $N_{c,o} = 80$.

4) To guarantee stability and a smooth reference current, the prediction and control horizons, $N_{p,o}$ and $N_{c,o}$, are designed larger than the inner loop predictive and control horizon, respectively [31].
5) To guarantee a good dynamic response, the outer loop settling time is adjusted at least 20 times greater than the inner control loop settling time.

B. Stability Analysis

Based on the singular perturbation theory [37], the outer control loop stability and the inner control loop stability can be analyzed separately. In this part, the impacts of both MPC loop parameters on the system stability will be analyzed. The stability analysis is based on the closed-loop pole placement of the inner and outer loops, respectively.

The inner control loop stability analysis has been developed from the closed-loop poles using the model described in (8) and (9), and as a function of the control effort parameter $r_{\omega,i}$, the prediction and control horizons $N_{p,i}$ and $N_{c,i}$, and the electrical parameters listed in Table I.

Fig. 2 shows the position of the inner closed-loop poles for different prediction and control horizons and sweeping the control effort, $r_{\omega,i}$, from 0 to 100. In Fig. 2(a), the prediction and control horizons are selected as $N_{p,i} = 2$ and $N_{c,i} = 1$, respectively. For these horizons, when $r_{\omega,i}$ increases, the poles move close to the unitary circle; thus, for high control effort, the system may become unstable. Conversely, in Fig. 2(b), the prediction and control horizons are selected as $N_{p,i} = 8$ and $N_{c,i} = 4$, respectively. It should be noted that the stability is ensured for all the control effort, $r_{\omega,i}$, range. Therefore, $N_{p,i} = 8$ and $N_{c,i} = 4$ are selected for the controller implementation.

On the other hand, the outer control loop stability analysis has been developed from the closed-loop poles using the model described in (14) and (15) and as a function of the control parameters.

Fig. 3 shows the position of the outer closed-loop poles for different prediction and control horizons and sweeping the control effort, $r_{\omega,o}$, from 10^6 to 10^{10}. In Fig. 3(a), the prediction and control horizons are selected as $N_{p,o} = 40$ and $N_{c,o} = 8$, respectively. For these horizons, the poles are unstable for a wide range of $r_{\omega,o}$. Instead, in Fig. 3(b), the prediction and control horizons are selected as $N_{p,o} = 400$ and $N_{c,o} = 80$, respectively. As can be seen, the stability is ensured for a wide range of control effort, $r_{\omega,o}$. Besides, an increment in the control effort makes the control action less aggressive, which results in a slower transient response. Finally, based on the placement of the poles, $N_{p,o} = 400$ and $N_{c,o} = 80$ are selected for the controller implementation.

C. Inner Loop Parameter Selection

The inner loop control effort is designed according to the dynamic specifications presented above using the closed-loop eigenvalues (28) and the system parameters listed in Table I.

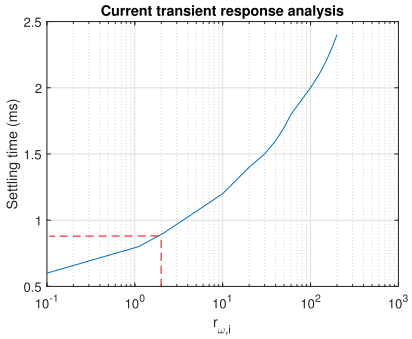

Fig. 4. Inner loop settling time for $r_{\omega,i}$ variation from 0 to 100.

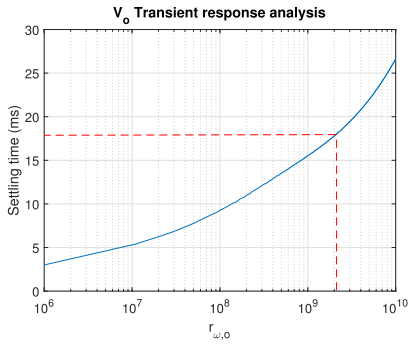

Fig. 5. V_o settling time for $r_{\omega,o}$ variation from 10^6 to 10^{10}.

As previously stated, the prediction and control horizons, $N_{p,i}$ and $N_{c,i}$, have been selected as $N_{c,i} = 4$ and $N_{p,i} = 8$, respectively. From these parameters, the selected closed-loop poles are obtained. The suitable value of the control effort $r_{\omega,i}$ is designed according to the desired position of the closed-loop eigenvalues (28) according to dynamic specifications 2 and 3 presented in the design guideline.

Fig. 4 shows the transient response of the inner control loop for a control effort variation in the range $0 \leq r_{\omega,i} \leq 100$. As can be seen, with increasing control effort, the settling time increases. The selected control and prediction horizons combined with a control effort $r_{\omega,i} = 2$ allow a theoretical settling time of 0.9 ms and a damping ratio of 0.730. Moreover, these parameters lead to a stable system with a fast transient response, as verified experimentally in Section VII.

D. Outer Loop Parameter Selection

As has been stated previously, the prediction and control horizons, $N_{p,o}$, and $N_{c,o}$, are adjusted to ensure a smooth reference current. Besides, the control effort parameter, $r_{\omega,o}$, for the outer control loop has been adjusted according to the desired position of the closed-loop eigenvalues (28) according to dynamic specification 4 presented in the design guideline. According to the aforementioned considerations and the theoretical inner loop settling time of 0.9 ms, the outer loop must be designed with a settling time greater than 18 ms.

In order to ensure smooth reference current, the control and prediction horizons are selected as $N_{c,o} = 80$ and $N_{p,o} = 400$, respectively. Fig. 5 shows transient response of the outer loop for a control effort variation in the range $10^6 \leq r_{\omega,o} \leq 10^{10}$. As can be seen, for a lower control effort, the controller transient response is faster, and in the range $r_{\omega,o} \leq 2 \times 10^9$, the settling time is less than 18 ms; hence, the third design specification is not accomplished. The selected control and prediction horizons combined with a control effort $r_{\omega,o}= 3 \times 10^9$ deal with a theoretical settling time of approximately 19.5 ms. Moreover, these parameters lead to a stable system with an excellent transient response, as verified experimentally in Section VII.

V. Lyapunov-Based Analysis

Based on [38], this section deals with the stability analysis and robustness of the proposed controller under electrical parameter uncertainties. For this purpose, the incremental control (25) is rewritten as

$$\Delta \mathbf{u}(k) = \mathbf{K}_r(\mathbf{y}^*(k) - \mathbf{y}(k)) - \mathbf{K}_x \Delta \mathbf{x}_m(k) \tag{29}$$

where $\mathbf{y}^*(k)$ is the reference vector, and the gain of the controller can be expressed in a vector form as $\mathbf{K}_c = [\mathbf{K}_x \ \mathbf{K}_r]$. According to the last expression, it holds that

$$\Delta \mathbf{u}(k) = -\mathbf{K}_c \tilde{\mathbf{x}}(k) \tag{30}$$

where

$$\tilde{\mathbf{x}}(k) = [\Delta \mathbf{x}_m(k) \ \ \mathbf{y}(k) - \mathbf{y}^*(k)]^T. \tag{31}$$

Now, to analyze the proposed control under parameter uncertainties, the closed-loop equation may be rewritten in the following manner [39]:

$$\begin{aligned} \tilde{\mathbf{x}}(k+1) &= ((\mathbf{A} + \Delta \mathbf{A}) - (\mathbf{B} + \Delta \mathbf{B})\mathbf{K}_c)\tilde{\mathbf{x}}(k) \\ &= (\tilde{\mathbf{A}} - \tilde{\mathbf{B}}\mathbf{K}_c)\tilde{\mathbf{x}}(k) \end{aligned} \tag{32}$$

where $\mathbf{A}$ and $\mathbf{B}$ are the matrices of the nominal model, and $\Delta \mathbf{A}$ and $\Delta \mathbf{B}$ regard to the model uncertainties. According to the definition in (31), the cost function defined in (54) can be rewritten as a discrete-time linear–quadratic regulator (LQR)

$$\begin{aligned} J_{\text{opt}} = &\sum_{m=1}^{N_p} \tilde{\mathbf{x}}_{\text{opt}}^T(k+m|k)\tilde{\mathbf{x}}_{\text{opt}}(k+m|k) \\ &+ \sum_{m=0}^{N_c-1} \Delta \mathbf{u}_{\text{opt}}^T(k+m|k) r_\omega \Delta \mathbf{u}_{\text{opt}}(k+m|k). \end{aligned} \tag{33}$$

Since the above equation is quadratic, it can be used as a Lyapunov candidate for the stability analysis. Then, defining the Lyapunov function as

$$V(\tilde{\mathbf{x}}(k), k) = J_{\text{opt}} \tag{34}$$

and taking into account that in the classic MPC, the stability is achieved if the Lyapunov function decreases along the state trajectory, we can write

$$V(\tilde{\mathbf{x}}(k+1), k+1) - V(\tilde{\mathbf{x}}(k), k) < 0. \tag{35}$$

Using (30), (32), (34), and (35), the following stability condition is obtained:

$$(\tilde{\mathbf{A}} - \tilde{\mathbf{B}}\mathbf{K}_c)^T(\tilde{\mathbf{A}} - \tilde{\mathbf{B}}\mathbf{K}_c) - \mathbf{K}_c^T r_\omega \mathbf{K}_c - \mathbf{I} < 0. \tag{36}$$

TASK : Controller(h)

/* The predictive model and the controller gains $\mathbf{K}_{r,i}$, $\mathbf{K}_{c,i}$, $\mathbf{K}_{h,i}$, $\mathbf{K}_{r,o}$, $\mathbf{K}_{c,o}$ and $\mathbf{K}_{h,o}$ are calculated offline with Matlab functions */
/* Sampling and processing */
$(v_{abc}, i_{abc}, v_o, i_o)$ = ReadADC()
$(v_d(k), v_q(k))$ = ABCtoDQ(v_{abc})
$(i_d(k), i_q(k))$ = ABCtoDQ(i_{abc})
/*Outer loop predictive model */
$\mathbf{x}_{m,o}(k) = v_o^2$
$\Delta\mathbf{x}_{m,o}(k) = \mathbf{x}_{m,o}(k) - \mathbf{x}_{m,o}(k-1)$
$\mathbf{d}_o(k) = v_o i_o$
$\Delta\mathbf{d}_o(k) = \mathbf{d}_o(k) - \mathbf{d}_o(k-1)$
$\mathbf{x}_o(k) = [\Delta\mathbf{x}_{m,o}(k) \;\; v_o^2]$
/* Optimum reference currents calculation */
$\Delta i_d^*(k) = \mathbf{K}_{r,o} {v_o^*}^2 - \mathbf{K}_{c,o}\mathbf{x}_o(k) - \mathbf{K}_{h,o}\Delta\mathbf{d}_o(k)$
$i_d^*(k) = \Delta i_d^*(k) + i_d^*(k-1)$
$i_q^*(k) = 0$
/* Predictive model and estimation of $\mathbf{x}_{m,i} = [i_d \;\; i_q]$ */
$\hat{\mathbf{x}}_{m,i}(k) = \mathbf{A}_{m,i}\hat{\mathbf{x}}_{m,i}(k-1) + \mathbf{B}_{m,i}\mathbf{u}_i(k-1) + \mathbf{L}_{obs}([i_d(k); i_q(k)] - \mathbf{C}_{m,i}\hat{\mathbf{x}}_{m,i}(k-1))$
$\Delta\mathbf{x}_{m,i}(k) = \hat{\mathbf{x}}_{m,i}(k) - \hat{\mathbf{x}}_{m,i}(k-1)$
$\mathbf{d}_i(k) = [v_d(k); v_q(k)]$
$\Delta\mathbf{d}_i(k) = \mathbf{d}_i(k) - \mathbf{d}_i(k-1)$
$\mathbf{x}_i(k) = [\Delta\mathbf{x}_{m,i}(k) \;\; \hat{\mathbf{x}}_{m,i}(k)]$
/* Optimum control signal calculation */
$\Delta\mathbf{u}_i(k) = \mathbf{K}_{r,i}[i_d^*(k); i_q^*(k)] - \mathbf{K}_{c,i}\mathbf{x}_i(k) - \mathbf{K}_{h,i}\Delta\mathbf{d}_i(k)$
$\mathbf{u}_i(k) = \Delta\mathbf{u}_i(k) + \mathbf{u}_i(k-1)$
$(m_d(k), m_q(k))$=$\mathbf{u}_i(k)$
(T_{abc}) = SpaceVectorPWM(m_d, m_q)

Fig. 6. Pseudocode of the controller task.

Equation (36) shows that the stability is affected by the parameter uncertainties and depends on $\mathbf{K}_c$ and, as a consequence, on the parameter selection.

Equation (36) can be computed for both loops using the corresponding system parameters $\mathbf{A}_i, \mathbf{B}_i$, and $\mathbf{K}_{c,i}$ for the inner loop and $\mathbf{A}_o, \mathbf{B}_o$, and $\mathbf{K}_{c,o}$ for the outer loop, with the system parameters and control gains shown in Table I.

To analyze the robustness of the proposed control under grid impedance uncertainties, the stability condition (36) is evaluated for different values of L. Thus, substituting into (36) the values of the system parameters and inner loop control gains shown in Table I and Section IV and sweeping L from 0.01 to 50 mH, it is found that the system is stable as long as the grid inductance $L > 1.9$ mH. Furthermore, the same analysis could be done to analyze the robustness of the proposed control under the dc-link capacitance uncertainties. Therefore, substituting into (36) the values of the system parameters and outer loop control gains shown in Table I and Section IV, it is found that the system is stable as long as the dc-link capacitance satisfies the following condition: $C > 100\,\mu$F. The robustness against other system and control parameters can be numerically evaluated following this procedure.

VI. Controller Implementation

This section presents the implementation of the proposed cascade MPC shown in Fig. 1. Fig. 6 shows the pseudocode for the proposed controller implementation. The subindexes o and i represent the outer loop and inner loop control variables, respectively. In this proposal, the controller uses two unconstrained linear MPCs for the outer and inner loops, respectively. Hence, the optimization problem can be solved offline, as it happens in an LQR, reducing the computational burden of the control algorithm. According to that, all the matrices and gains, i.e., $\mathbf{K}_{r,o}$, $\mathbf{K}_{c,o}$, $K_{h,o}$, $\mathbf{K}_{r,i}$, $\mathbf{K}_{c,i}$, and $\mathbf{K}_{h,i}$, are computed offline with customized MATLAB functions, as shown in Appendix B. Once the gains are obtained, the algorithm is executed as shown in Fig. 6. The algorithm starts with the acquisition of the variables v_o, i_o, i_a, i_b, i_c, v_a, v_b, and v_c. The dq components of the grid currents and voltages are computed using a phase-locked loop (PLL). At this stage, the two MPC algorithms are applied. On the one hand, the UPFR variables v_o and i_o are used to obtain the outer state-space vectors $\mathbf{x}_o(k)$ and $\Delta\mathbf{d}_o(k)$. To regulate the output dc-link voltage, the reference current i_d^* is obtained applying (23). On the other hand, a KF estimator (24) is used to generate the estimated dq grid-side currents and voltages and to compensate the computational delay [35]. These estimated variables allow us to obtain the new space-state vector $\mathbf{x}_i(k)$. Finally, this vector is used to obtain the control signals, $m_d(k)$ and $m_q(k)$, implemented in the SVM and provide fixed switching frequency (see Fig. 6).

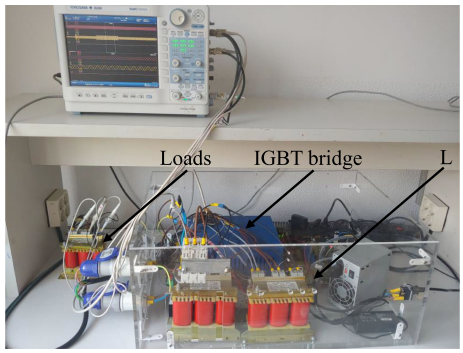

Fig. 7. Photograph of the experimental setup.

VII. Experimental Validation

This section presents the experimental tests implemented on a three-phase rectifier prototype that is shown in Fig. 7. It was built using a 2.3-kVA Guasch MTL-CBI0060F12IXHF full bridge as the power converter and a TMS320F28M36 floating-point DSP as the control platform with a sampling frequency of 10 kHz. The grid voltages have been generated using a PACIFIC 360-AMX source. The system parameters are listed in Table I.

In order to exhibit the performances of the proposed cascade CCS-MPC scheme and to compare to recent MPC approaches, a robust adaptive FCS-MPC [18] and a cascade FCS-MPC [19] are also carried out in the experimental tests.

The robust adaptive FCS-MPC [18] inner loop is based on a cost function evaluation to minimize the active and reactive power error obtaining the optimal voltage vector. Besides, an MRAS estimator based on the Lyapunov function is used in the inner loop to improve robustness against uncertainties parameters. Moreover, a PI controller is used in the outer loop to regulate

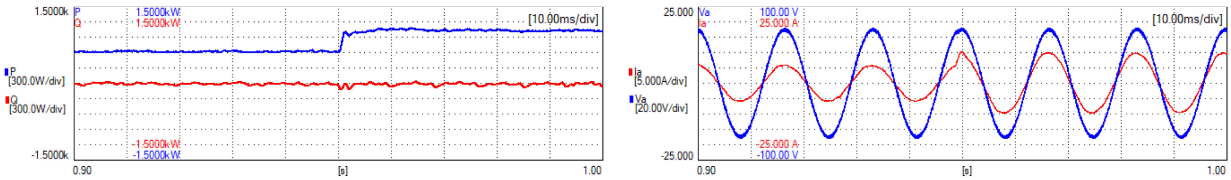

(a) (b)

Fig. 8. Performance evaluation of the proposed controller. (a) Active power (300 W/div) and reactive power (300 W/div). (b) Grid-side current (5 A/div) and grid voltage (20 V/div) for phase leg A.

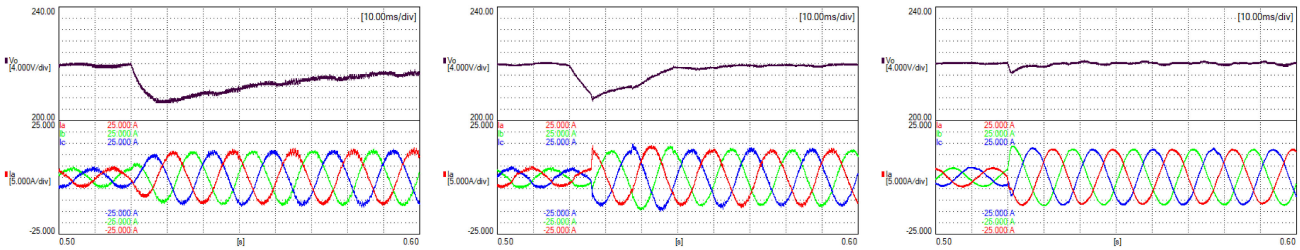

(a) (b) (c)

Fig. 9. Experimental results for output voltage (4 V/div) and three-phase grid-side currents (5 A/div) with a load step change from 132 to 44 Ω. (a) Robust adaptive FCS-MPC [18]. (b) Cascade FCS-MPC [19]. (c) Proposed controller.

the output voltage. It worth noting that the PI controller has been designed in order to obtain a good dynamic performance with the lowest grid current harmonic content.

On the other hand, the cascade FCS-MPC [19] inner loop is based on a cost function evaluation to minimize the grid current error obtaining the optimal voltage vector. Furthermore, the outer loop consists of an optimization problem that is solved online to obtain the inner loop reference minimizing the output voltage error.

However, since the controllers presented in [18] and [19] are based on FCS-MPC, the switching frequency is variable. Hence, for a fair comparison, a KF estimator is used in both control methods with a sampling frequency of 40 kHz to reduce the current ripple and to obtain higher performance [40].

A. *UPFR Performance Evaluation*

To validate the capability to provide a desired unity PF of the proposed control scheme, on the one hand, Fig. 8(a) shows the active and reactive powers using the proposed cascade CCS-MPC in the presence of sudden load changes. As can be observed, the reactive power is approximately zero; besides, the transient response is very fast, and a negligible reactive power deviation arises when the load change is produced. On the other hand, Fig. 8(b) shows the grid-side current and the grid voltage in phase leg A. As can be seen, the two signals are in phase, thus providing a unity PF, as desired.

B. *Transient Response During Load Step Changes*

To validate the dynamic performance of the proposed control scheme and the performed design, the controller presented in [18] and [19] and the proposed controller have been tested in the case of a load step change from 132 to 44 Ω. Fig. 9(a)–(c) shows the dynamic response of the output voltage and the grid-side currents using [18] and [19] and the proposed cascade CCS-MPC, respectively. Fig. 9(a) shows a significant voltage deviation and slow dynamic response using [18], with a voltage drop of 14 V and a settling time of approximately 80 ms. In Fig. 9(b), a faster output dynamic response using [19] with a settling time of approximately 30 ms can be observed. However, a significant output voltage deviation is produced, with a voltage drop of 12 V. Instead, using the proposed cascade CCS-MPC, it results in an insignificant voltage deviation with the fastest dynamics response, with a voltage drop of only 3.5 V and a settling time of approximately 20 ms, as has been stated in the control design. Furthermore, the switching frequency spectra using [18] and [19] and the proposed controller are shown in Fig. 10. It should be noted that the proposed controller achieve a fixed switching frequency. Instead, the authors of [18] and [19] present a variable switching frequency as had been stated, with a switching frequency concentrated between 14–20 and 10–15 kHz, respectively. Moreover, the measured spectra of the currents using [18] and [19] and the proposed controller are shown in Fig. 11. Note that the proposed control provides a lower harmonic distortion, with a THD of 1.71%. To sum up, the proposed controller operates with a high performance without increasing the computational burden and with a fixed switching frequency.

C. *Parameter Uncertainty Robustness*

In order to test the robustness of the proposed controller against parameter uncertainties, the methods presented in [18] and [19] and the proposed cascade CCS-MPC have been tested in the presence of a grid inductance variation and a capacitance variation of the dc capacitor.

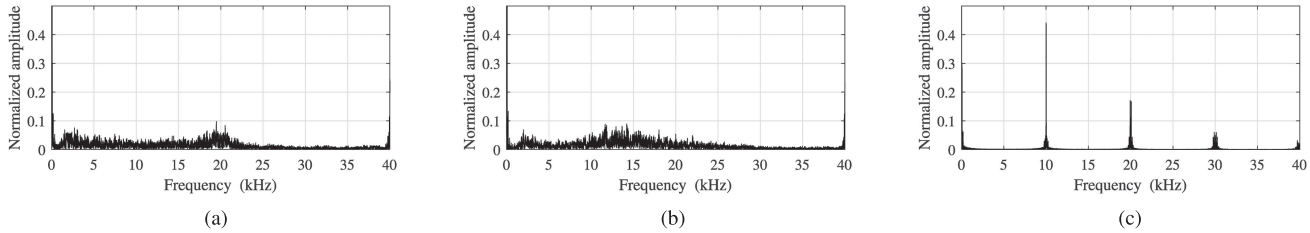

Fig. 10. Experimental switching frequency spectrum with amplitude relative to fundamental. (a) Robust adaptive FCS-MPC [18]. (b) Cascade FCS-MPC [19]. (c) Proposed controller.

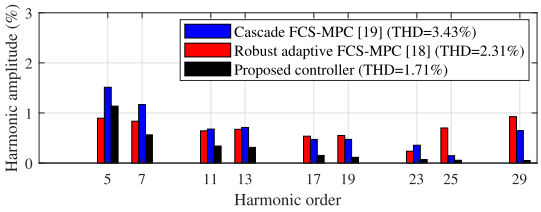

Fig. 11. Measured spectra of grid currents.

First, the three control methods assume a nominal grid inductance value of 5 mH, and they were tested for an inductance of 60% of the nominal value. Fig. 12(a)–(c) shows the dynamics of output voltage and the grid-side currents of the considered control schemes with a grid inductance of 3 mH. It should be noted that the cascade FCS-MPC [19] is unstable in the presence of the grid inductance variation. However, the robust adaptive FCS-MPC [18] and the proposed control remain stable for the grid inductance mismatch.

Second, to validate the robustness against capacitance mismatches, the dc capacitor in the control algorithms are set to 700 μF, while the nominal dc capacitor remains 1000 μF. Fig. 13(a)–(c) shows the dynamics of output voltage and the grid-side currents of the considered control schemes with the capacitance mismatch. From Fig. 13, a slight increase in both the voltage deviation and the settling time during the load change should be noted. Consequently, the capacitance mismatches have a small effect on the dynamic performance of the proposed controller, thus validating the robustness of the proposed control against parameter uncertainties.

D. Transient Response During Unbalanced Voltage Sags

Finally, the proposed controller has been tested under a grid voltage unbalance. Fig. 14 shows the performances of [18] and [19] and the proposed cascade CCS-MPC controller under a grid voltage sag. This sag is characterized by positive and negative sequences $V^+ = 0.65$ p.u. and $V^- = 0.15$ p.u., respectively, and with a phase angle between sequences of $\phi = \pi/6$.

Fig. 14(a) shows the output voltage and the grid voltages and currents during the grid voltage sag using the robust adaptive FCS-MCP [18]. It can be seen that a voltage deviation appears in the output voltage when the voltage sag is produced. Moreover, the grid-side currents are clearly distorted due to the voltage sag, with a THD of 18.7%. The same waveforms are shown in Fig. 14(b) but using the cascade FCS-MPC [19]. It should be noted that a voltage deviation appears in the output voltage when the voltage sag is produced. Moreover, the cascade FCS-MPC presents a steady-state deviation in the output voltage during the voltage sag, with a voltage error of 3 V. Besides, the grid-side currents are distorted, with a THD of 9.5%. Finally, Fig. 14(c) shows the output voltage and the grid voltages and currents during the grid voltage sag using the proposed controller. When the voltage sag is produced, the output voltage has an insignificant voltage deviation. Moreover, the currents track the unbalanced grid voltages during the sag, and the distortions in the grid-side currents are clearly reduced, with a THD of 4.2%. It should be noted that the steady-state performance has not been affected by the voltage sag. Thus, the robustness of the proposed controller under external disturbance has been validated.

E. Computational Burden Analysis

This subsection presents a comparative of the computational burden. The comparative includes the switching frequency, algorithm execution time, and computational load (CL), obtained as follows:

$$\mathrm{CL}(\%) = f_s \times \Sigma(t_{\mathrm{ex},j}) \times 100 \tag{37}$$

where $t_{\mathrm{ex},j}$ is the execution time of each task in the controller.

A DSP timer is used to measure the time of each controller task. Fig. 15 shows the execution times for the different tasks of each controller. The execution time of the MPC schemes is described as follows.

1) Time of the robust adaptive FCS-MPC [18] includes the outer loop PI controller, inductance estimation, prediction states, the cost function evaluation, and the selection of the optimal voltage vectors.
2) Time of the cascade FCS-MPC [19] includes the MPC outer loop, a PLL, prediction states, the cost function evaluation, and the selection of the optimal voltage vectors.
3) Time of the proposed cascade CCS-MPC includes a PLL, the outer state-space vector computation, reference current calculation (23), a KF estimator, the control signal calculation (20), and time for the SVM.

Note that the execution time is not very different for the three tested schemes. However, the sampling frequency in [18] and [19] is 40 kHz with a variable switching frequency. Besides, the proposed control operates with a fixed switching frequency and a sampling frequency of 10 kHz, reducing the CL. Table II shows the comparison among the three tested schemes.

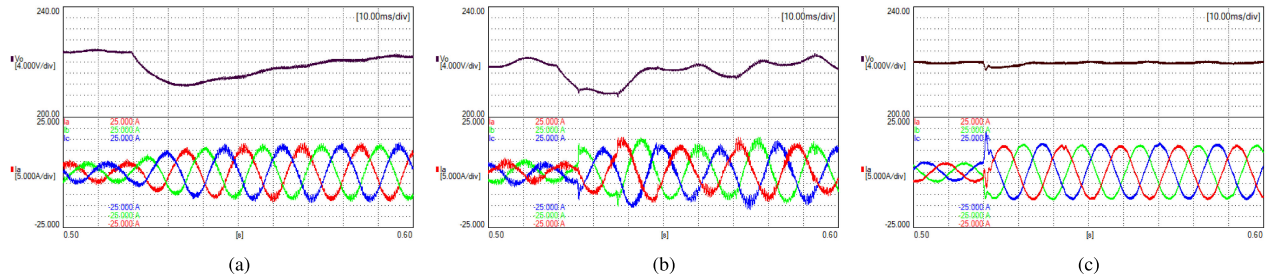

(a) (b) (c)

Fig. 12. Experimental results for output voltage (4 V/div) and three-phase grid-side currents (5 A/div) with 60% inductance of the nominal value. (a) Robust adaptive FCS-MPC [18]. (b) Cascade FCS-MPC [19]. (c) Proposed controller.

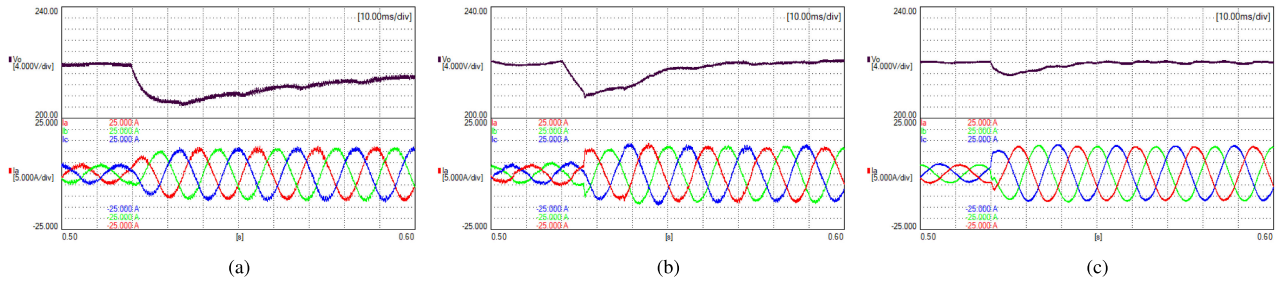

(a) (b) (c)

Fig. 13. Experimental results for output voltage (4 V/div) and three-phase grid-side currents (5 A/div) with 70% capacitance of the nominal value. (a) Robust adaptive FCS-MPC [18]. (b) Cascade FCS-MPC [19]. (c) Proposed controller.

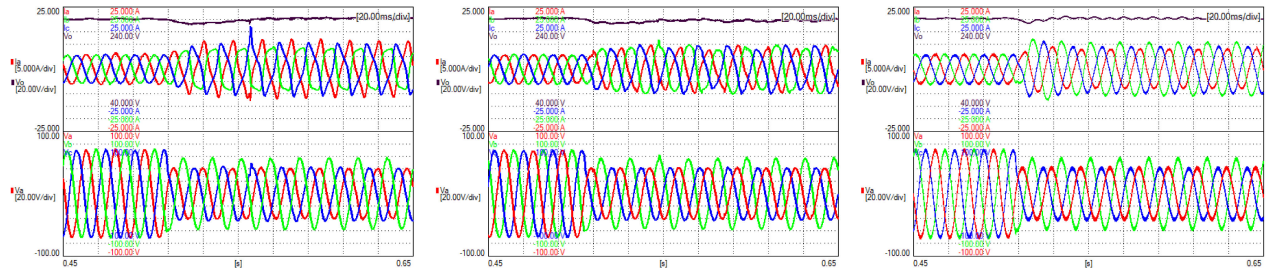

(a) (b) (c)

Fig. 14. Output voltage (20 V/div) and three-phase currents (5 A/div) and voltage (20 V/div) waveforms during a voltage sag. (a) Robust adaptive FCS-MPC [18]. (b) Cascade FCS-MPC [19]. (c) Proposed controller.

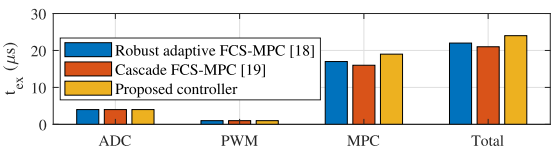

Fig. 15. Computing execution times for the tested control schemes.

TABLE II
COMPARATIVE ANALYSIS

Controller	f_s	f_{sw}	t_{ex}	CL
[18]	40 kHz	Variable	22 μs	88%
[19]	40 kHz	Variable	21 μs	84%
proposal	10 kHz	10 kHz	24 μs	24%

VIII. CONCLUSION

As a novelty, a cascade dual-mode predictive control for a three-phase UPFR has been proposed, with the following properties. On the one hand, the proposed inner loop controller uses a reduced model with an embedded integrator to achieve a zero steady-state error and robustness against grid voltage sags and model parameter uncertainties. A fixed switching frequency is achieved since an SVM is used. On the other hand, the outer control loop uses a linear model to generate the optimal reference currents and achieves a zero steady-state output voltage error. The experimental results show that the proposed control improves the transient voltage response in the presence of sudden load step changes with negligible voltage deviation. The experimental results have also shown the proposed control robustness against parameter uncertainties. Finally, the experimental results showed that the proposed control works correctly even in the

case of grid voltage sags. As an open topic for future research, the application of the proposed predictive control to other power converters can be studied. Active power filters and multilevel topologies are some interesting candidates. Furthermore, the parallel connection of these topologies can be considered to increase capacity and allow modularity.

APPENDIX A

This Appendix deals with the derivation of the incremental model. This model contains an embedded integrator, which is useful to eliminate the steady-state errors.

Given a space-state model defined by

$$\mathbf{x}_m(k+1) = \mathbf{A}_m\mathbf{x}_m(k) + \mathbf{B}_m\mathbf{u}(k) + \mathbf{D}_m\mathbf{d}(k) \tag{38}$$

$$\mathbf{y}_m(k) = \mathbf{C}_m\mathbf{x}_m(k) \tag{39}$$

the incremental model can be obtained by taking a difference operation on both sides of (38), as follows:

$$\mathbf{x}_m(k+1) - \mathbf{x}_m(k) = \mathbf{A}_m(\mathbf{x}_m(k) - \mathbf{x}_m(k-1)) + \mathbf{B}_m(\mathbf{u}(k) - \mathbf{u}(k-1)) + \mathbf{D}_m(\mathbf{d}(k) - \mathbf{d}(k-1)).$$

Besides, denoting the incremental state variable as

$$\Delta\mathbf{x}_m(k+1) = \mathbf{x}_m(k+1) - \mathbf{x}_m(k)$$

$$\Delta\mathbf{x}_m(k) = \mathbf{x}_m(k) - \mathbf{x}_m(k-1)$$

and the incremental control signal and disturbance variable by

$$\Delta\mathbf{u}_m(k) = \mathbf{u}_m(k) - \mathbf{u}_m(k-1)$$

$$\Delta\mathbf{d}_m(k) = \mathbf{d}_m(k) - \mathbf{d}_m(k-1)$$

the incremental model is obtained as

$$\Delta\mathbf{x}_m(k+1) = \mathbf{A}_m\Delta\mathbf{x}_m(k) + \mathbf{B}_m\Delta\mathbf{u}(k) + \mathbf{D}_m\Delta\mathbf{d}(k). \tag{40}$$

Note that $\Delta\mathbf{u}(k)$ is the control signal in the incremental state-space model.

The same procedure is applied to the output variable, yielding

$$y(k+1) - y(k) = \mathbf{C}_m(\mathbf{x}_m(k+1) - \mathbf{x}_m(k)) = \mathbf{C}_m(\mathbf{A}_m\Delta\mathbf{x}_m(k) + \mathbf{B}_m\Delta u(k) + \mathbf{D}_m\Delta\mathbf{d}(k)) \tag{41}$$

or equivalently

$$y(k+1) = y(k) + \mathbf{C}_m(\Delta\mathbf{x}_m(k+1)). \tag{42}$$

Note that (42) denotes the presence of an integrator in the system.

Now, a new state-space vector that contains the incremental variables $\Delta\mathbf{x}_m(k)$ and the output $y(k)$ can be defined as follows:

$$\mathbf{x}(k) = [\Delta\mathbf{x}_m(k) \;\; y(k)]^T. \tag{43}$$

Combining both (40) and (41) results in the augmented state-space model, expressed as

$$\mathbf{x}(k+1) = \mathbf{A}\mathbf{x}(k) + \mathbf{B}\Delta\mathbf{u}(k) + \mathbf{D}\Delta\mathbf{d}(k) \tag{44}$$

$$y(k) = \mathbf{C}\mathbf{x}(k) \tag{45}$$

where the matrices of the augmented model, i.e., $\mathbf{A}$, $\mathbf{B}$, $\mathbf{C}$, and $\mathbf{D}$, can be expressed as a function of the matrices $\mathbf{A}_m, \mathbf{B}_m, \mathbf{C}_m$, and $\mathbf{D}_m$, yielding

$$\mathbf{A} = \begin{pmatrix} \mathbf{A}_m & \mathbf{0}_{p\times q} \\ \mathbf{C}_m\mathbf{A}_m & \mathbf{I}_{q\times q} \end{pmatrix}, \quad \mathbf{B} = \begin{pmatrix} \mathbf{B}_m \\ \mathbf{C}_m\mathbf{B}_m \end{pmatrix}$$

$$\mathbf{C} = \begin{pmatrix} \mathbf{0}_{q\times p} & \mathbf{I}_{q\times q} \end{pmatrix}, \quad \mathbf{D} = \begin{pmatrix} \mathbf{D}_m \\ \mathbf{C}_m\mathbf{D}_m \end{pmatrix}$$

with $\mathbf{I}$ being the identity matrix and $\mathbf{0}$ a square matrix of zeros; p is the number of state variables and q is the number of outputs.

APPENDIX B

Let us consider the vector of future incremental control signals at the sampling instant k_j expressed as follows:

$$\Delta\mathbf{u} = [\Delta u(k_j) \; \Delta u(k_j+1) \; \ldots \; \Delta u(k_j+N_c-1)]^T \tag{46}$$

where N_c is the control horizon. With the given information $x(k_j)$, the future state variables can be predicted for a prediction horizon, N_p. Note that N_p is also the length of the optimization window. Considering an incremental state-space model defined by the matrices $\mathbf{A}$, $\mathbf{B}$, and $\mathbf{C}$, where the vector $\mathbf{d}(k)$ in (44) is the disturbance vector, the future state variables can be computed sequentially according to (46)

$$\begin{aligned}\mathbf{x}(k_j+N_p|k_j) = {} & \mathbf{A}^{N_p}\mathbf{x}(k_j) + \mathbf{A}^{N_p-1}\mathbf{B}\Delta u(k_j) \\ & + \mathbf{A}^{N_p-1}\mathbf{D}\Delta d(k_j)\ldots \\ & \ldots + \mathbf{A}^{N_p-N_c}\mathbf{B}\Delta u(k_j+N_c-1) \\ & + \mathbf{A}^{N_p-N_c}\mathbf{D}\Delta d(k_j+N_c-1)\end{aligned} \tag{47}$$

where $\mathbf{x}(k_j+N_p|k_j)$ is the predicted state variable at k_j+N_p from the system information $\mathbf{x}(k_j)$. In the same way, the predicted outputs can be obtained from the predicted state variables as follows:

$$\begin{aligned}y(k_j+N_p|k_j) = {} & \mathbf{C}\mathbf{A}^{N_p}\mathbf{x}(k_j) + \mathbf{C}\mathbf{A}^{N_p-1}\mathbf{B}\Delta u(k_j) \\ & + \mathbf{C}\mathbf{A}^{N_p-1}\mathbf{D}\Delta d(k_j)\ldots \\ & \ldots + \mathbf{C}\mathbf{A}^{N_p-N_c}\mathbf{B}\Delta u(k_j+N_c-1) \\ & + \mathbf{C}\mathbf{A}^{N_p-N_c}\mathbf{D}\Delta d(k_j+N_c-1).\end{aligned} \tag{48}$$

It can be seen that all the predicted variables are expressed in terms of the current state variables $\mathbf{x}(k_j)$ and the future control trajectory $\Delta\mathbf{u}$. The output vector y is defined as

$$\mathbf{y} = [y(k_j+1|k_i) \; y(k_j+2|k_i) \; \ldots \; y(k_j+N_p|k_j)]^T. \tag{49}$$

Expressing the aforementioned relations in a compact matrix form, it gives

$$\mathbf{y} = \mathbf{F}\mathbf{x}(k_j) + \mathbf{G}\Delta\mathbf{u} + \mathbf{H}\Delta\mathbf{d} \tag{50}$$

where $\mathbf{F}$ is a vector of dimension N_p and $\mathbf{G}$ and $\mathbf{H}$ are matrices of dimension $N_c \times N_p$, written, respectively, as

$$\mathbf{F} = \left(\mathbf{C}\mathbf{A}\mathbf{C}\mathbf{A}^2\mathbf{C}\mathbf{A}^3\cdots\mathbf{C}\mathbf{A}^{N_p}\right)^T \tag{51}$$

$$\mathbf{G} = \begin{pmatrix} \mathbf{CB} & \mathbf{0}_{q\times q} & \cdots & \mathbf{0}_{q\times q} \\ \mathbf{CAB} & \mathbf{CB} & \cdots & \mathbf{0}_{q\times q} \\ \vdots & \vdots & \ddots & \vdots \\ \mathbf{CA}^{N_p-1}\mathbf{B} & \mathbf{CA}^{N_p-2}\mathbf{B} & \cdots & \mathbf{CA}^{N_p-N_c}\mathbf{B} \end{pmatrix} \tag{52}$$

$$\mathbf{H} = \begin{pmatrix} \mathbf{CD} & \mathbf{0}_{q\times q} & \cdots & \mathbf{0}_{q\times q} \\ \mathbf{CAD} & \mathbf{CD} & \cdots & \mathbf{0}_{q\times q} \\ \vdots & \vdots & \ddots & \vdots \\ \mathbf{CA}^{N_p-1}\mathbf{D} & \mathbf{CA}^{N_p-2}\mathbf{D} & \cdots & \mathbf{CA}^{N_p-N_c}\mathbf{D} \end{pmatrix} \tag{53}$$

where q is the number of outputs. In this case, in the inner loop, $q = 2$, and in the outer loop, $q = 1$. Define the objective function as

$$\mathbf{J} = ||(\mathbf{y}^* - \mathbf{y})||^2 + \Delta\mathbf{u}^T\mathbf{R}\Delta\mathbf{u} \tag{54}$$

where $\mathbf{R} = r_\omega \mathbf{I}_{pN_c\times pN_c}$ is a diagonal matrix, p is the number of outputs, $r_\omega > 0$ is the control effort used as a tuning parameter to adjust a desired closed-loop performance, and $\mathbf{y}^*$ is the reference vector. Note that in the case where the reference current is maintained practically constant inside the predictive window, $\mathbf{y}^*$ can be expressed as follows:

$$\mathbf{y}^*(k_j) = [\underbrace{\mathbf{I}_{q\times q}\ \ \mathbf{I}_{q\times q}\ \ \ldots\ \ \mathbf{I}_{q\times q}}_{N_p}]\mathbf{r}(k_j) \tag{55}$$

where $\mathbf{r}(k_j) = [y^*(k_j)]$ is the reference vector at the sampling instant k_j, the size of which is the prediction horizon N_p. Then, by taking the derivative of $\mathbf{J}$ with respect to $\Delta\mathbf{u}$, we obtain

$$\frac{\partial \mathbf{J}}{\partial \Delta\mathbf{u}} = -2\mathbf{G}^T(\mathbf{y}^* - \mathbf{F}\mathbf{x}(k_j) - \mathbf{H}\Delta\mathbf{d}(k_j)) + 2\mathbf{M}\Delta\mathbf{u} \tag{56}$$

where $\mathbf{M} = \mathbf{G}^T\mathbf{G} + \mathbf{R}$. By equalizing (56) to zero and taking into account the optimal control vector in (55), the following expression for the incremental control signals is obtained:

$$\Delta\mathbf{u}(k_j) = \mathbf{M}^{-1}\mathbf{G}^T(\bar{\mathbf{r}}y^*(k_j) - \mathbf{F}\mathbf{x}(k_j) - \mathbf{H}\Delta\mathbf{d}(k_j)). \tag{57}$$

Note that the vector $\Delta\mathbf{u}$ contains all the incremental control values from the sampling instant k_j to $k_j + N_c - 1$. Since (44), (45) is a time-invariant system, the incremental control can be expressed in terms of a state feedback controller. According to the definition in (46), the actual incremental control signal can be expressed as follows:

$$\begin{aligned}\Delta\mathbf{u}(k_j) &= \mathbf{K}_r y^*(k_j) - \mathbf{K}_c\mathbf{x}(k_j) - \mathbf{K}_h\Delta\mathbf{d}(k_j) \\ &= \mathbf{K}_r(y^*(k_j) - \mathbf{y}(k_j)) - \mathbf{K}_x\Delta\mathbf{x}_m(k_j) - \mathbf{K}_h\Delta\mathbf{d}(k_j)\end{aligned} \tag{58}$$

where

$$\mathbf{K}_r = \mathbf{W}(\mathbf{G}^T\mathbf{G} + \mathbf{R})^{-1}\mathbf{G}^T\bar{\mathbf{r}} \tag{59}$$

$$\mathbf{K}_c = \mathbf{W}(\mathbf{G}^T\mathbf{G} + \mathbf{R})^{-1}\mathbf{G}^T\mathbf{F} \tag{60}$$

$$\mathbf{K}_h = \mathbf{W}(\mathbf{G}^T\mathbf{G} + \mathbf{R})^{-1}\mathbf{G}^T\mathbf{H}. \tag{61}$$

Note that $\mathbf{K}_c = [\mathbf{K}_x\ \ \mathbf{K}_r]$ is the gain of the model-predictive controller. Besides, based on the receding horizon principle, $\mathbf{W}$ is the N_c-dimensional matrix $[\mathbf{I}_{p\times p}\ \mathbf{0}_{p\times p}\ \ldots\ \mathbf{0}_{p\times p}]$. Finally, the optimum control signal is obtained by adding the incremental value, $\Delta\mathbf{u}(k_j)$, to the control signal in the previous sampling instant, $\mathbf{u}(k_j - 1)$. Then, one has

$$\mathbf{u}(k_j) = \Delta\mathbf{u}(k_j) + \mathbf{u}(k_j - 1) \tag{62}$$

or equivalently

$$\begin{aligned}\mathbf{u}(k_j) = \mathbf{u}(k_j - 1) &+ \mathbf{K}_r(y^*(k_j) - \mathbf{y}(k_j)) - \mathbf{K}_x\Delta\mathbf{x}_m(k_j) \\ &- \mathbf{K}_h\Delta\mathbf{d}(k_j).\end{aligned} \tag{63}$$

It should be noted that $\mathbf{K}_r(y^*(k_j) - \mathbf{y}(k_j))$ is integrating the error, thus achieving zero steady-state error.

REFERENCES

[1] A. Prasad, P. Ziogas, and S. Manias, "An active power factor correction technique for three-phase diode rectifiers," *IEEE Trans. Power Electron.*, vol. 6, no. 1, pp. 83–92, Jan. 1991.

[2] B. A. Mather and D. Maksimović, "A simple digital power-factor correction rectifier controller," *IEEE Trans. Power Electron.*, vol. 26, no. 1, pp. 9–19, Jan. 2011.

[3] E. L. M. Mehl and I. Barbi, "An improved high-power factor and low-cost three-phase rectifier," *IEEE Trans. Ind. Appl.*, vol. 33, no. 2, pp. 485–492, Mar. 1997.

[4] Y.-W. Cho, J.-M. Kwon, and B.-H. Kwon, "Single power-conversion ac-dc converter with high power factor and high efficiency," *IEEE Trans. Power Electron.*, vol. 29, no. 9, pp. 4797–4806, Sep. 2014.

[5] Z. Yin, J. Liu, and Y. Zhong, "Study and control of three-phase PWM rectifier based on dual single-input single-output model," *IEEE Trans. Ind. Inform.*, vol. 9, no. 2, pp. 1064–1073, May 2013.

[6] R. Guzman, L. G. de Vicuña, J. Morales, M. Castilla, and J. Matas, "Sliding-mode control for a three-phase unity power factor rectifier operating at fixed switching frequency," *IEEE Trans. Power Electron.*, vol. 31, no. 1, pp. 758–769, Jan. 2016.

[7] J. Liu, Y. Gao, W. Luo, and L. Wu, "Takagi-Sugeno fuzzy-model-based control of three-phase AC/DC voltage source converters using adaptive sliding mode technique," *IET Control Theory Appl.*, vol. 11, no. 8, pp. 1255–1263, 2017.

[8] J. Liu, S. Vazquez, L. Wu, A. Marquez, H. Gao, and L. G. Franquelo, "Extended state observer-based sliding-mode control for three-phase power converters," *IEEE Trans. Ind. Electron.*, vol. 64, no. 1, pp. 22–31, Jan. 2017.

[9] H. Yang, Y. Zhang, J. Liang, J. Liu, N. Zhang, and P. D. Walker, "Robust deadbeat predictive power control with a discrete-time disturbance observer for PWM rectifiers under unbalanced grid conditions," *IEEE Trans. Power Electron.*, vol. 34, no. 1, pp. 287–300, Jan. 2019.

[10] Y. Zhang, J. Liu, H. Yang, and S. Fan, "New insights into model predictive control for three-phase power converters," *IEEE Trans. Ind. Appl.*, vol. 55, no. 2, pp. 1973–1982, Mar./Apr. 2019.

[11] A. Bouafia, J.-P. Gaubert, and F. Krim, "Predictive direct power control of three-phase pulsewidth modulation (PWM) rectifier using space-vector modulation (SVM)," *IEEE Trans. Power Electron.*, vol. 25, no. 1, pp. 228–236, Jan. 2010.

[12] Y. Gui, M. Li, J. Lu, S. Golestan, J. M. Guerrero, and J. C. Vasquez, "A voltage modulated DPC approach for three-phase PWM rectifier," *IEEE Trans. Ind. Electron.*, vol. 65, no. 10, pp. 7612–7619, Oct. 2018.

[13] S. Vazquez *et al.*, "Model predictive control: A review of its applications in power electronics," *IEEE Ind. Electron. Mag.*, vol. 8, no. 1, pp. 16–31, Mar. 2014.

[14] P. Kou, D. Liang, J. Li, L. Gao, and Q. Ze, "Finite-control-set model predictive control for DFIG wind turbines," *IEEE Trans. Autom. Sci. Eng.*, vol. 15, no. 3, pp. 1004–1013, Jul. 2018.

[15] D. E. Quevedo, R. P. Aguilera, M. A. Perez, P. Cortes, and R. Lizana, "Model predictive control of an AFE rectifier with dynamic references," *IEEE Trans. Power Electron.*, vol. 27, no. 7, pp. 3128–3136, Jul. 2012.

[16] S. Kouro, P. Cortes, R. Vargas, U. Ammann, and J. Rodriguez, "Model predictive control—A simple and powerful method to control power converters," *IEEE Trans. Ind. Electron.*, vol. 56, no. 6, pp. 1826–1838, Jun. 2009.

[17] Y. Zhang, Z. Wang, J. Jiao, and J. Liu, "Grid-voltage sensorless model predictive control of three-phase PWM rectifier under unbalanced and distorted grid voltages," *IEEE Trans. Power Electron.*, vol. 35, no. 8, pp. 8663–8672, Aug. 2020.
[18] M. Mehreganfar, M. H. Saeedinia, S. A. Davari, C. Garcia, and J. Rodriguez, "Sensorless predictive control of AFE rectifier with robust adaptive inductance estimation," *IEEE Trans. Ind. Inform.*, vol. 15, no. 6, pp. 3420–3431, Jun. 2019.
[19] J. Sawma, F. Khatounian, E. Monmasson, L. Idkhajine, and R. Ghosn, "Cascaded dual-model-predictive control of an active front-end rectifier," *IEEE Trans. Ind. Electron.*, vol. 63, no. 7, pp. 4604–4614, Jul. 2016.
[20] L. Tarisciotti *et al.*, "Model predictive control for shunt active filters with fixed switching frequency," *IEEE Trans. Ind. Appl.*, vol. 53, no. 1, pp. 296–304, Jan./Feb. 2017.
[21] T. H. Nguyen and K.-H. Kim, "Finite control set model predictive control with modulation to mitigate harmonic component in output current for a grid-connected inverter under distorted grid conditions," *Energies*, vol. 10, Feb. 2017, Art. no. 907.
[22] M. Trabelsi, S. Bayhan, K. A. Ghazi, H. Abu-Rub, and L. Ben-Brahim, "Finite-control-set model predictive control for grid-connected packed-u-cells multilevel inverter," *IEEE Trans. Ind. Electron.*, vol. 63, no. 11, pp. 7286–7295, Nov. 2016.
[23] L. Wang, *Model Predictive Control System Design and Implementation Using MATLAB*. Berlin, Germany: Springer, 2009.
[24] M. Ramzi, H. Youlal, and M. Haloua, "State space model predictive control of an aerothermic process with actuators constraints," *Intell. Control Autom.*, vol. 3, no. 1, pp. 50–58, Feb. 2012.
[25] L. Qian, L. Zhang, Q. Chen, and S. Quan, "Constrained model predictive control for a three-phase PWM rectifier," in *Proc. Chin. Autom. Congr.*, Oct. 2017, pp. 6745–6749.
[26] R. Guzman, L. G. de Vicuña, A. Camacho, J. Miret, and J. M. Rey, "Receding-horizon model-predictive control for a three-phase VSI with an LCL filter," *IEEE Trans. Ind. Electron.*, vol. 66, no. 9, pp. 6671–6680, Sep. 2019.
[27] J. H. Lee, "Model predictive control: Review of the three decades of development," *Int. J. Control, Autom. Syst.*, vol. 9, no. 3, Jun. 2011, Art. no. 415.
[28] J. Qin and T. Badgwell, "A survey of industrial model predictive control technology," *Control Eng. Pract.*, vol. 11, pp. 733–764, 2003.
[29] A. A. Ahmed, B. K. Koh, and Y. I. Lee, "A comparison of finite control set and continuous control set model predictive control schemes for speed control of induction motors," *IEEE Trans. Ind. Inform.*, vol. 14, no. 4, pp. 1334–1346, Apr. 2018.
[30] S. Golestan, E. Ebrahimzadeh, J. M. Guerrero, and J. C. Vasquez, "An adaptive resonant regulator for single-phase grid-tied VSCs," *IEEE Trans. Power Electron.*, vol. 33, no. 3, pp. 1867–1873, Mar. 2018.
[31] J. Rossiter, *Model-Based Predictive Control: A Practical Approach*. Boca Raton, FL, USA: CRC Press 2003.
[32] C.-M. Ying, S. Voorakaranam, and B. Joseph, "Analysis and performance of the LP-MPC and QP-MPC cascade control system," in *Proc. Amer. Control Conf.*, 1998, vol. 2, pp. 806–810.
[33] K. V. Ling, W. Bingfang, H. Minghua, and Z. Yu, "A model predictive controller for multirate cascade systems," in *Proc. Amer. Control Conf.*, 2004, vol. 2, pp. 1575–1579.
[34] A. Isidori, *Nonlinear Control Systems*. New York, NY, USA: Springer-Verlag, 1995.
[35] K. H. Ahmed, A. M. Massoud, S. J. Finney, and B. W. Williams, "Sensorless current control of three-phase inverter-based distributed generation," *IEEE Trans. Power Del.*, vol. 24, no. 2, pp. 919–929, Apr. 2009.
[36] K. Ogata, *Modern Control Engineering*, 4th ed. Englewood Cliffs, NJ, USA: Prentice-Hall, 2001.
[37] P. Kokotovic, H. Khalil, and J. O'Reilly, *Singular Perturbation Methods in Control: Analysis and Design*. New York, NY, USA: Academic, 1986.
[38] W.-H. Chen, "Stability analysis of classic finite horizon model predictive control," *Int. J. Control Autom. Syst.*, vol. 8, no. 2, pp. 187–197, 2010.
[39] R. Guzman, L. G. de Vicuña, M. Castilla, J. Miret, and J. de la Hoz, "Variable structure control for three-phase LCL-filtered inverters using a reduced converter model," *IEEE Trans. Ind. Electron.*, vol. 65, no. 1, pp. 5–15, Jan. 2018.
[40] P. Karamanakos and T. Geyer, "Guidelines for the design of finite control set model predictive controllers," *IEEE Trans. Power Electron.*, vol. 35, no. 7, pp. 7434–7450, Jul. 2020.

Carlos Alfaro was born in San Salvador, El Salvador. He received the B.S. degree in mechanical engineering from the Universidad Centroamericana "José Simeón Cañas," San Salvador, in 2015, and the M.S. degree in automatic systems and industrial electronics engineering in 2018 from the Technical University of Catalonia, Vilanova i la Geltrú, Spain, where he is currently working toward the Ph.D. degree in electronics with the Department of Electronic Engineering.

His current research interests include power electronics, nonlinear, and predictive control.

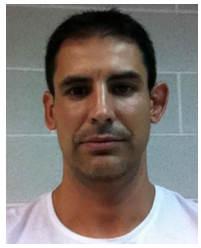

Ramon Guzman (Member, IEEE) received the B.S., M.S., and Ph.D. degrees in telecommunications engineering from the Technical University of Catalonia, Barcelona, Spain, in 1999, 2004, and 2016, respectively.

He is currently an Associate Professor with the Department of Automatic Control, Technical University of Catalonia, Vilanova i la Geltrú, Spain. His research interests include nonlinear and adaptive control for three-phase power converters.

Dr. Guzman is a member of the Renewable Energy Systems Subcommittee of Power Electronics Technical Committee of the IEEE Industrial Electronics Society. He is an Associate Editor for IEEE TRANSACTIONS ON INDUSTRIAL ELECTRONICS.

Luis Garcia de Vicuña received the Ingeniero de Telecomunicación and Dr.Ing. degrees in telecommunication engineering from the Technical University of Catalonia, Barcelona, Spain, in 1980 and 1990, respectively, and the Dr.Sci. degree from the Université Paul Sabatier, Toulouse, France, in 1992.

He is currently a Full Professor with the Department of Electronic Engineering, Technical University of Catalonia, Vilanova i la Geltrú, Spain, where he teaches courses on power electronics. His research interests include power electronics modeling, simulation and control, active power filtering, and high-power-factor ac–dc conversion.

Jaume Miret (Member, IEEE) received the B.S. degree in telecommunications, the M.S. degree in electronics, and the Ph.D. degree in electronics from the Universitat Politecnica de Catalunya, Barcelona, Spain, in 1992, 1999, and 2005, respectively.

From 1993 to 2011, he was an Assistant Professor with the Department of Electronic Engineering, Universitat Politecnica de Catalunya, Vilanova i la Geltrú, Spain, where he has been an Associate Professor since 2011. His research interests include dc-to-ac converters, active power filters, and digital control.

Miguel Castilla received the B.S., M.S., and Ph.D. degrees in telecommunication engineering from the Technical University of Catalonia, Barcelona, Spain, in 1988, 1995, and 1998, respectively.

Since 2019, he has been a Full Professor with the Department of Electronic Engineering, Technical University of Catalonia, Vilanova i la Geltrú, Spain, where he teaches courses on control of power electronic converters. His research interests include power electronics, control, renewable energy systems, and electrical microgrids.